Accepted to J. Chem. Phys. 10.1063/5.0142483

Polarity-dependence of the nonlinear dielectric response in interfacial water

N. Mulpuri and D. Bratko*

Department of Chemistry, Virginia Commonwealth University, Richmond, Virginia 23221, United States

Abstract

Molecular dynamics simulations are used to study nonlinear dielectric responses of a confined aqueous film in a planar nanopore under perpendicular electric fields at varied voltages between confining graphene sheets. Dielectric saturation reminiscent of the bulk phase behavior is prevalent at very strong fields, whereas we observe a nonmonotonic permittivity dependence on electric field at intermediate strengths where field-alignment and spontaneous polarization of interfacial water are of comparable magnitudes. The coupling between the two effects results in distinct dielectric responses at opposite confinement walls. The normal component of both the differential dielectric constant and dielectric difference constant tensors averaged over the region closer to the wall under incoming electric field (field pointing from the liquid to the solid phase) initially *increases* with the strength of the imposed field. The differential permittivity peaks at a field strength previously shown to offset the surface-induced orientation bias of hydration molecules at this wall. Further strengthening of the field results in conventional saturation behavior. At the opposite wall (subject to outgoing field) and in the central region of water slab, the nonlinear dielectric response resembles bulklike saturation. The conditions at the permittivity extremum coincide with the window of accelerated reorientation rates of interfacial water molecules under incoming field uncovered in earlier molecular dynamics analyses.

*dbratko@vcu.edu

I. Introduction

Electrified solid/water interfaces are ubiquitous in biological systems and in a host of electrochemical applications. Experiments and molecular simulations reveal significant deviations from bulk water permittivity in the proximity of confining surfaces[1-13]. Dielectric screening in interfacial water is strongly anisotropic and the permittivity tensor components show nonmonotonic variation with the distance from the solid surface [14]. [5-7, 15-20]. In nanosized pores, the anisotropy extends over the entire aqueous film with the spatially-averaged normal component typically below the permittivity of the parallel component and below the isotropic permittivity of the bulk phase. In simulation studies, dielectric behavior of confined water was deduced from correlated polarization fluctuations or from polarization changes under comparatively weak fields[5, 6, 8, 21, 22] predominantly concerning linear response regimes of both the parallel and normal permittivity components. The present study includes stronger electric fields leading to pronounced deviations from the linear regime and nonmonotonic saturation effects. We focus on the comparison between the field-strength dependences of the normal permittivity component at two opposing pore walls revealing a striking difference between nonlinear responses to fields of opposite directions *relative* to the walls (incoming or outgoing fields pointing from the liquid phase towards the wall, or from the wall to the liquid, respectively[23]). Because of molecular asymmetry and optimization of hydrogen bonding, interfacial water has long been known to undergo spontaneous polarization in the absence of external field[24-26]. In a planar confinement under a normal field, spontaneous polarization facilitates molecular alignment with the perpendicular field at one of the walls while weakening it at the other one[23, 27-29]. Our calculations quantify distinct dielectric responses at the opposite walls in terms of the microscopic analogue of dielectric constant averaged over hydration layers at the confinement walls subject to incoming field at one side and outgoing field on the other. The difference between the responses to incoming and outgoing fields is most visible at intermediate field strengths with comparable magnitudes of spontaneous and field-induced contributions to the overall polarization. The asymmetry in total polarization responses to the field is negligible at vanishing field strengths but remains notable in the strong field limit because opposite polarization signs at zero field support different maximal polarization-changes at opposing walls.

II. Model and Methods

The model system consists of approximately five layers of water molecules, confined between two parallel graphene sheets separated by a distance D = 18.62 Å (Fig. 1). Each graphene sheet is comprised of 364 carbon atoms. In analogy to earlier work[30], the walls were built by using the nanotube builder module of VMD program[31]. Graphene sheets are positioned along x-y plane and electric field is applied along z axis normal to the sheets. To model a semi-infinite system, the walls and intervening liquid are periodically replicated in lateral (x,y) directions. The structure of the walls is fixed during entire simulation. To facilitate comparisons with earlier studies of field effects in aqueous confinements[5-9, 11, 13, 15, 27, 32-34], water is modeled using the SPC/E potential[35], known to reproduce well the dielectric properties of bulk water[36]. To obtain a glimpse into the

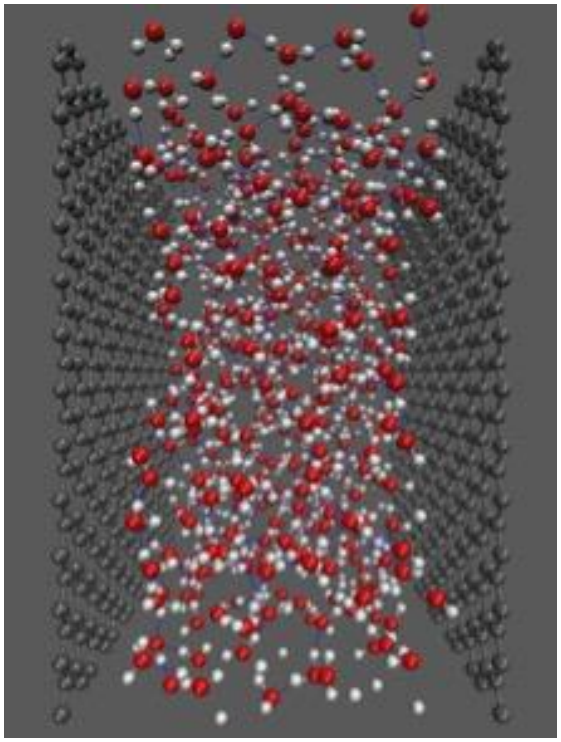

Fig. 1 A snapshot of the aqueous layer consisting of 458 water molecules between parallel graphene sheets of size 29.8 x 32.1 Å^2 at the separation d_z=18.62 Å. To model a semi-infinite confinement, the system is periodically replicated in parallel (xy) directions.

possible role of molecular polarizability, we repeated the simulation for a couple of systems using the SWM4-NDP model of water[37]. Water-wall carbon interactions were described by the Lennard-Jones potential with carbon length and energy parameters 3.58 Å and 0.277 kJ mol^{-1}, which give the nonpolar walls contact angle near 90°[38, 39]. The number of water molecules, N_{H2O}=458, corresponds to the average amount of water inside the field-free model pore open to exchange with bulk aqueous phase at ambient conditions in a lengthy Grand Canonical Monte Carlo simulation using the code from earlier works[40, 41]. In all subsequent runs with or without the field, we used canonical (N,V,T) Molecular Dynamics simulations. At zero electric field, water distributions at the two interfaces are symmetric and feature identical time-averaged properties. The symmetry breaks down after the imposition of the electric field (Fig. 2).

Molecular dynamics simulations are performed in the canonical (N,V,T) ensemble at T = 300 K using GROMACS package[42]. Equations of motion are integrated with the leapfrog algorithm with a time step of 1 fs. Initially, the system energy is minimized using the steepest descent method with $5{\cdot}10^4$ steps and tolerance 10^3 kJ mol^{-1} nm^{-1}. The minimization is followed by equilibration for 11 ns, and 16 or more ns for production. Lennard-Jones interactions and real-space Coulombic terms are truncated beyond 10 Å. The long-range electrostatic interactions are calculated using the particle mesh Ewald (PME) summation[43] with fast Fourier transform (FFT) grid spacing of 0.16 nm. Thermostatting relies on velocity rescaling[44] with a stochastic term and a 100 fs time constant. To account for the two-dimensional periodicity of the system, electrostatic interactions are calculated in a periodic system with empty space inserted between the box replicas in z direction (increasing the effective size of the simulation box along z axis by a factor of three) along with the approximate slab correction[45], which implies vacuum boundary conditions in the normal (z) direction[46]. LINCS algorithm[47, 48] is used to maintain SPC/E water molecule rigidity. Configurations are collected every 2 fs. The simulation box dimensions in x and y directions are L_x = 32.1 Å, L_y = 29.8 Å and in z-direction (excluding the space between periodic replicas) L_z = 22.0Å. In the absence of the field, this width was sufficient to reproduce the hydration layer atom density and angle distribution profiles from a preceding study[23]. To secure numerical accuracy of single and double integrals of rapidly varying charge density profiles required the use of very small bins for density calculations. 1760 bins along z axis were used after confirming essentially identical results with 880 and 1760 bins using either trapezoidal or Simpson integration. A set of distinct voltages across the confinement corresponds to a sequence of electric displacements D_z

corresponding to hypothetical (vacuum) field strengths E_o=$D_z\varepsilon_o^{-1}$ of magnitudes 0.0, 0.025, 0.05, 0.08, 0.11, 0.15, 0.2, 0.3, 0.5 and 0.7 VÅ^{-1} where ε_o denotes the permittivity of vacuum. Reflecting the layered molecular ordering of the solvent, the actual field pervading the aqueous film features a strong oscillatory dependence on the position z [5-7, 15-20], with the *average* field strength vastly reduced due to dielectric screening. In given range of fields, the effective dielectric constants (see below) averaged across the aqueous film (the region with nonzero atom and charge densities), $\varepsilon_{eff} = <\frac{1}{\varepsilon_z(z)}>^{-1}$, varies from ~13 (at strongest fields) to ~25 in vanishing field. The screening restricts the *mean* strength of the remaining field inside the film below ~ 0.05 VÅ^{-1}, far from the decomposition value of ~ 0.25-0.3 VÅ^{-1} applicable [49, 50] to deionized water at perfect insulation. To characterize the magnitude of electric perturbation in terms of an experimentally accessible quantity, and to provide a connection with simulations performed[51] using constant potential Molecular Dynamics[52, 53], we use simulated charge density profiles to determine the voltage U across the confinement. Fig. 2 and Table 1 list mean voltages between graphene sheets corresponding to the solution of Poisson's equation for mean atom-charge distributions at preselected electrical displacements.

III. Results and discussion

A. Structure and polarization

Fig. 2 illustrates the layering of confined water in terms of mean number densities of oxygen and hydrogen atoms along the normal (z) direction at voltages between the confining surfaces $U_{C\text{-}C}$ = 0.0, -0.0705, -0.225, -0.428, -0.889, and -2.326 V. For easier reading, we omitted results for the remaining voltages $U_{C\text{-}C}$ = -0.14, -0.310, -0.577, and -1.578 V, which can be found in Fig. S1 in the Supplementary Material. As the two walls are identical, the structure in the field-free system (black lines) is entirely symmetric. Introduction of an aligning field perpendicular to the walls, however, renders the structure increasingly asymmetric as spontaneous polarization of water next to confining walls[24-26] cooperates with field alignment under outgoing field (pointing from the wall into the liquid) while opposing it in the outgoing field at the opposite wall. To optimize hydrogen bonding, hydration water favors near-parallel water/dipole/wall orientations with a moderate bias toward dipoles pointing away from the walls[23]. In the present system (Fig. 1), the field points from left to right, *i.e.* in outgoing direction at the left and incoming at the right

surface. Consistent with previous works[23, 27, 29], the favorable coupling between the two orienting effects in the outgoing field results in increased oxygen and hydrogen density peaks at the left

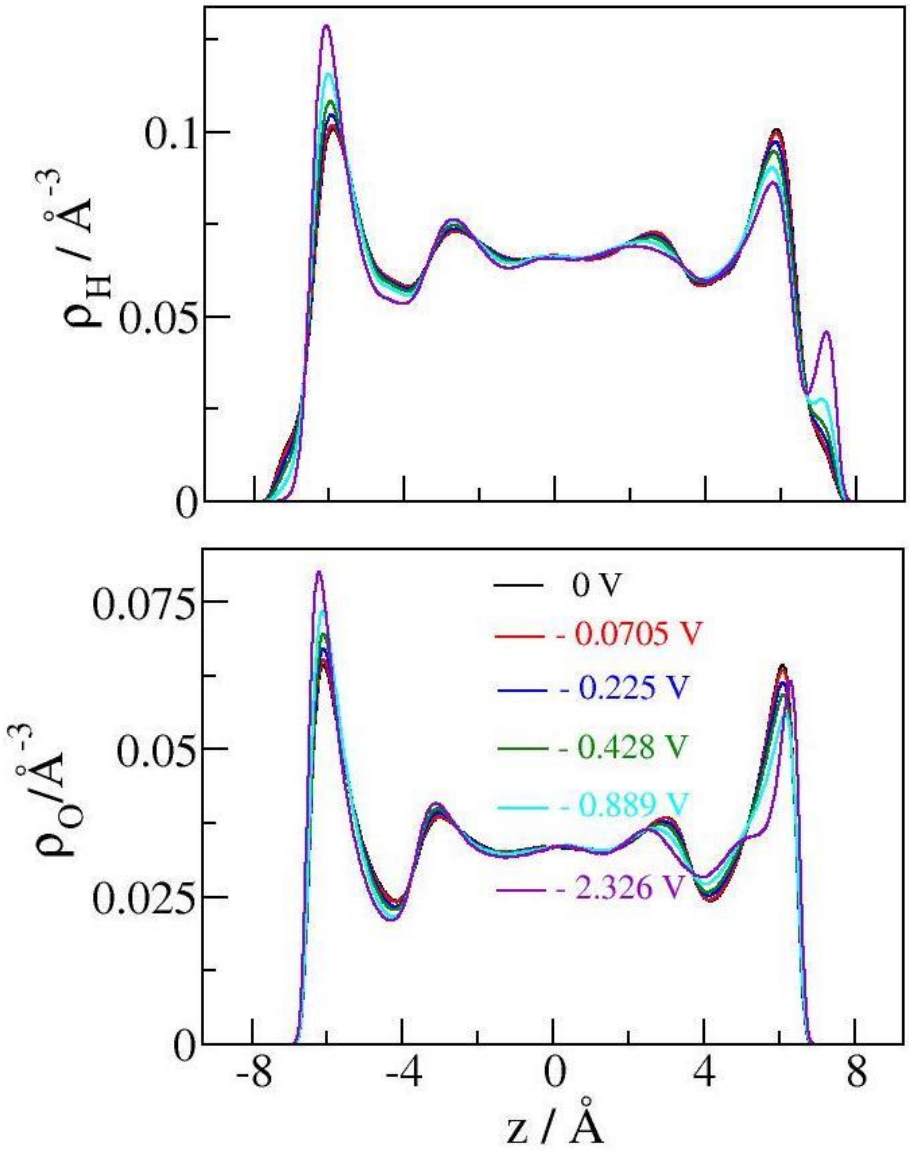

Fig. 2 Density profiles of water oxygen (bottom) and hydrogen atoms (top) in the model nanopore at different voltages between parallel graphene sheets positioned at z=±9.31Å. Positive electric field is pointing from left to right wall with reported voltages corresponding to the difference between mean electrostatic potentials $U = \psi_{right} - \psi_{left}$. Unless stated otherwise, identical color-voltage relation is used throughout the entire manuscript.

wall. At the same time, we observe a gradual emergence of a new hydrogen density peak next to the right wall (Fig. 2). Structural changes underlie asymmetric charge redistributions resulting in uneven dielectric responses next to the walls. Mean charge density profiles corresponding to atom distributions from Fig. 2 are illustrated in Fig. 3. Results for the remaining voltages are incorporated in Fig. S2 in the Supplementary Material.

In molecular simulations, time-averaged dielectric responses can be deduced from the polarization $\boldsymbol{m}(\boldsymbol{r})$ as a function of external field. While $\boldsymbol{m}(\boldsymbol{r})$ is a vectorial function of position, in this work, we focus on systems of planar geometry subject to a uniform external field normal to the walls where all relevant quantities depend only on the position z relative to the confinement walls. To characterize dielectric screening of a perpendicular field $\boldsymbol{E}(\boldsymbol{r})=(0, 0, E_z(z))$, we need to consider solely the normal (z) components of the field $\boldsymbol{E}$, polarization $\boldsymbol{m}$, and permittivity tensor $\boldsymbol{\varepsilon}$, $E_z(z)$, $m_z(z)$, and $\varepsilon_{zz}(z)$. As such we omit the component subscript (z) of these quantities in the remainder of the text and in Eqs. 1-7. According to the formalism of refs.[15,5] we define local polarization $m(z)$ in terms of instantaneous charge density $\rho_q(z)=\frac{1}{L_x L_y}\sum_i q_i\,\delta(z_i - z)$, where the

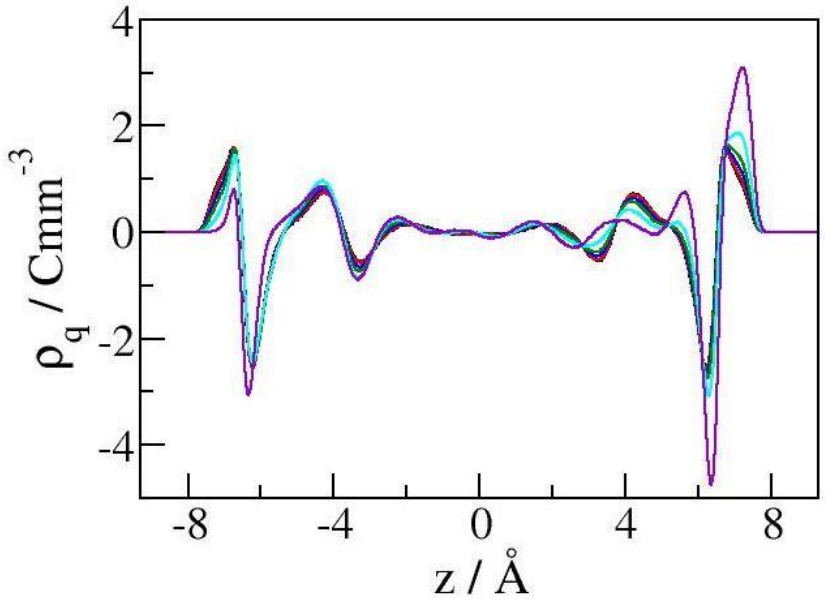

Fig. 3 Time-averaged charge-density profiles following from spatial distributions of partial charges on oxygen and hydrogen atoms of water at different voltages across the slit. The colors relate to the voltages shown in Fig. 2.

sum includes all molecular sites carrying charges q_i (oxygen or hydrogen atoms in case of SPC/E water) in the box:

$$m(z) = -\int_{-\infty}^{z} \rho_q(z')dz' \quad (1)$$

In contrast to molecular dipole density $P_1(z)$[54, 55], $m(z)$ in Eq. 1 includes contributions from molecular multipoles of all orders present in given liquid[5, 15]. While dipole density $\boldsymbol{P}_1(\boldsymbol{r})$ alone suffices in a fluid with *point dipoles* (*e.g.* Stockmayer liquid), expansion of $\boldsymbol{m}(z)$ in terms of multipole (dipole, quadrupole, octupole…) densities also reveals significant contributions from quadrupole and octupole terms, $\nabla\cdot\boldsymbol{P}_2(\boldsymbol{r})$ and $\nabla\nabla:\boldsymbol{P}_3(\boldsymbol{r})$, in simulations of confined water[15]. Eq. 1 comprises all terms by directly summing individual partial-charge contributions. The reader is referred to ref.[15] for in-depth discussion and rigorous derivations. In the Supplementary Material, we also include a quantitative comparison between complete $m(z)$ and dipole density $P_1(z)$ for our model system.

Fig. 4 shows polarization profiles corresponding to time-averaged charge density profiles illustrated in Fig. 3. Due to asymmetric density distributions and uneven molecular alignments at the two walls, a strong positive field can induce a bigger polarization change $\Delta m(z)$ at the wall under incoming field, *i.e.* at the right wall of our system.

Averaged profiles $\langle m(z)\rangle$ determine the voltages $U_{C\text{-}C}$, here reported as the difference between electrostatic potentials on the right and left sheet, $U_{C-C} = \psi_{right} - \psi_{left} = -\int_{z_l}^{z_r} E(z)dz = -\int_{z_l}^{z_r}\left[E_o - \frac{\langle m(z)\rangle}{\varepsilon_o}\right]dz$. Similarly, we obtain the voltage across the aqueous film of thickness d_f as $U_{film} = -\int_{-d_f/2}^{d_f/2}\left[E_o - \frac{\langle m(z)\rangle}{\varepsilon_o}\right]dz$. The average field strength across the entire slit, or across the aqueous film, are then given as $\langle E_{C-C}\rangle = \frac{U_{C-C}}{z_r - z_l}$ and $\langle E_{film}\rangle = \frac{U_{film}}{d_f}$. Above, $E_o = D_z\varepsilon_o^{-1}$ represents the vacuum field corresponding to the imposed electric displacement D_z, which can be interpreted as charge per unit area of a (implicit) capacitor maintaining the imposed external field. $E(z)$ represents the time-average of the actual, dielectrically screened electric field (determined from simulated $\langle m(z)\rangle$), and z_r and z_l denote graphene sheet positions in z dimension. In all cases we consider, $E_o \geq 0$, hence $\psi_{left} \geq \psi_{right}$. Table 1 and Fig. 2 list the values of U corresponding to preselected values of E_o and simulated $m(z)$. In analogy to earlier work[22], the

Table 1. Voltage U defined as the difference between mean electrostatic potentials at opposing graphene sheets $\psi_{right} - \psi_{left}$, vacuum field strength E_o and corresponding electric displacement $D_z=E_o\varepsilon_o$, average dielectrically screened field between carbon sheets, $\langle E_{C\text{-}C}\rangle$, and average field inside the aqueous film, $\langle E_{film}\rangle$. The film is defined as the region with nonzero atom density and associated charge density ρ_q.

U / V	$\langle E_o\rangle$ / VÅ^{-1}	D_z / μC cm^{-2}	$\langle E_{C\text{-}C}\rangle$ / VÅ^{-1}	$\langle E_{film}\rangle$ / VÅ^{-1}
-0.0705	0.025	0.22	0.0038	0.00097
-0.140	0.05	0.44	0.0075	0.00193
-0.225	0.08	0.71	0.0121	0.00308
-0.310	0.11	0.97	0.0166	0.00433
-0.428	0.15	1.33	0.023	0.00618
-0.577	0.20	1.77	0.031	0.00867
-0.889	0.30	2.66	0.0477	0.0144
-1.578	0.50	4.43	0.0847	0.0299
-2.326	0.70	6.20	0.140	0.0487

main contribution to reported voltages U corresponds to the dielectrically inert regions with $\varepsilon(z) = 1$, located between the positions of carbon atoms and the boundaries of the 'aqueous film'. The film is defined as the region with nonzero charge density $\rho_q(z)$ due to finite density of charged sites of water. Consistent with ref.[6], we consider film boundaries at the hydrogen-carbon distance of closest approach 1.09 Å from the carbon atom plane on each side of the confinement. The resulting film width of 16.4 Å was sufficient to contain all liquid atoms in the interior of the 'film' at any time while allowing hydrogen atoms to approach the film boundaries within ~0.1 Å or less at all simulation conditions. The potential drop across the inert layers on both sides (representing no more than 12% of entire pore width) varied from ~65% (in strong fields) to ~80% (at weak fields) of the total voltage between the carbon sheets. This translates to the *average field strength* across the aqueous film in the range of ~ 4% to 7% of the preselected vacuum field strengths E_o. Table 1 presents average values of the actual (dielectrically screened) field strengths $E_z(z;E_o)$ across the entire confinement, $\langle E_{C\text{-}C}\rangle$, and fields pervading the confined water film, $\langle E_{film}\rangle$, for all studied systems.

B. Dielectric behavior

Local permittivity of simulated water can be deduced from the time-averaged *change* of polarization, $\Delta m(z)$, induced by an externally applied electric displacement along z direction, D_z or vacuum field $E_o = D_z\varepsilon_o^{-1}$: $\Delta m(z;E_o) = < m(z;E_o) > - < m_o(z) >$. Average polarization profiles $< m(z;E_o) >$ for different values of E_o, and the zero-field profile $< m_o(z) >$ associated with interfacial structure of field-free (U=0) confined water, are shown in Fig. 4. Defining the (normal component) inverse dielectric constant in terms of the ratio of time-averaged local field change $\Delta E_z(z;E_o) = E_z(z;E_o) - E_z(z;0)$ and externally imposed electric displacement, $\frac{1}{\varepsilon(z)} = \frac{\varepsilon_o \Delta E_z(z;E_o)}{D_z} = \frac{\Delta E_z(z)}{E_o}$, and applying the Gauss law $\Delta E_z(z;E_o) = -\frac{\Delta m(z;E_o)}{\varepsilon_o}$ obtains the relation[5, 15, 55-57, 8,7]

$$\frac{1}{\varepsilon(z)} = 1 - \frac{\Delta m(z;E_o)}{D_z} = 1 - \frac{\Delta m(z;E_o)}{E_o \varepsilon_o} \tag{2}$$

Alternatively, $\frac{1}{\varepsilon(z)}$ can be determined from the correlation between *fluctuating* polarization $\boldsymbol{m}(\boldsymbol{r})$ and concurrent total polarization $\boldsymbol{M}=\int_V m(\boldsymbol{r})d\boldsymbol{r}$. In a planar slab under perpendicular field, the normal (z) component of $\boldsymbol{M}$=(0, 0, M) associated with a periodic box of lateral dimensions L_x and L_y and volume $V=L_xL_yL_z$ is

$$M = L_x L_y \int_{-\infty}^{\infty} m(z')dz' \ , \tag{3}$$

where we omit subscript z on m and M. With this definition, the fluctuation-dissipation relation for the normal component of permittivity[5, 15] can be written as

$$\frac{1}{\varepsilon(z)} = 1 - \frac{\beta}{\varepsilon_o} [\ <m(z)M> - <m(z)><M>] \tag{4}$$

where $$\beta\ [\ <m(z)M> - <m(z)><M>] = \frac{\partial}{\partial E_o} \frac{\int [\ m(z;E_o) - <m_o(z)>\ ] e^{-\beta(U-ME_o)} d\boldsymbol{X}}{\int e^{-\beta(U-ME_o)} d\boldsymbol{X}} = \frac{\partial \Delta m(z;E_o)}{\partial E_o} \tag{5}$$

In weak fields, $\frac{\partial \Delta m(z;E_o)}{\partial E_o} \approx \frac{\Delta m(z;E_o)}{E_o}$ independently of E_o (linear response regime). At these conditions, Eqs. 2 and 4 are equivalent and can be used interchangeably, and the averages $< >$ in Eq. 4 can be taken at E_o=0 [5, 15]. At stronger fields (nonlinear regime), $\frac{\partial \Delta m(z;E_o)}{\partial E_o}$ depends on the

strength of the field and the averages in Eq. 4 must be obtained at specified E_o. Here, the derivative $\frac{\partial \Delta m(z;E_o)}{\partial E_o} \equiv \beta$ [<$m(z)M$> - <$m(z)$><M>], Eqs. 4-5, no longer equals the finite difference ratio $\frac{\Delta m(z)}{E_o}$ used in Eq. 2. As such, Eq. 4 yields the inverse *differential* dielectric constant $\frac{1}{\varepsilon_d(z;E_o)} = 1 - \frac{\beta}{\varepsilon_o}$[<$m(z)M$> - <$m(z)$><$M$>] $= 1 - \frac{1}{\varepsilon_o}\left(\frac{\partial \Delta m(z;E_o)}{\partial E_o}\right)$. Eq. 2, on the other hand, yields the inverse *dielectric difference* constant[9] (also termed static dielectric constant[9, 58]), $\frac{1}{\bar{\varepsilon}(z;E_o)}$, which represents the average of $\frac{1}{\varepsilon_d(z;E_o)}$ over the field interval from zero to final E_o,

$$\frac{1}{\bar{\varepsilon}(z;E_o)} = \frac{1}{E_o}\int_0^{E_o} \frac{1}{\varepsilon_d(z;E_o')}\, dE_o', \tag{6}$$

Averaging the reciprocal value of ε_d, the relation between normal components of $\frac{1}{\varepsilon_d(z;E_o)}$ and $\frac{1}{\bar{\varepsilon}(z;E_o)}$ (Eq. 6) *differs* from the analogous expressions applicable in the bulk phase (and in lateral direction in confinement) where ε_d rather than its inverse is averaged over the field interval from zero to E_o[9].

Fig. 4 reveals prominent differences between polarization responses $\Delta m(z;U)$ at opposing walls of the confinement at high sheet-to-sheet voltages due to external field. In the absence of external field (black curve), polarization profiles in the two half-spaces are antisymmetric. Under

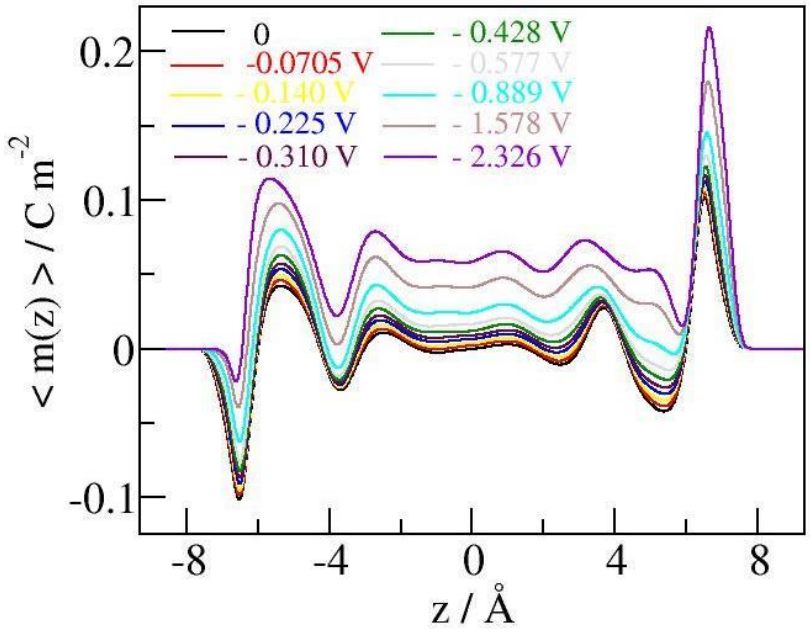

Fig. 4 Local polarization profiles inside the slit at different voltages across the nanopore.

positive fields (E_o>0), the increment $\Delta m(z, E_o)$ is generally positive but very nonuniform. The response is on overall stronger at the right wall (incoming field).

In the literature, polarization m(z) in nanoconfined water under the field is occasionally approximated by considering only the dipole contribution. Fig. S4 (Supplementary material) compares the latter approximation with the results of Eq. 1 at selected fields. Significant differences between the two approaches confirm the use of Eq. 1 is necessary for correct description of even qualitative features of the system, including the difference between polarizations under opposite (outgoing *vs*. incoming) directions of the field relative to confinement walls.

Asymmetric variation of $\Delta m(z, E_o)$ is reflected in uneven dielectric responses in left (outgoing field) and right (incoming field) portions of the aqueous slab. The inverse dielectric difference constant $\frac{1}{\bar{\varepsilon}(z;U)}$ (Eq. 2 and Fig. 5) features strong oscillations where regions with negative $\bar{\varepsilon}$ reveal local overscreening of external field ($\Delta m(z, E_o) > D = \varepsilon_o E_o$) [5, 7, 8, 15, 22, 55]. The ordered structure underlying the oscillatory character of $m(z)$ and $\frac{1}{\bar{\varepsilon}(z;U)}$ suggests the oscillatory

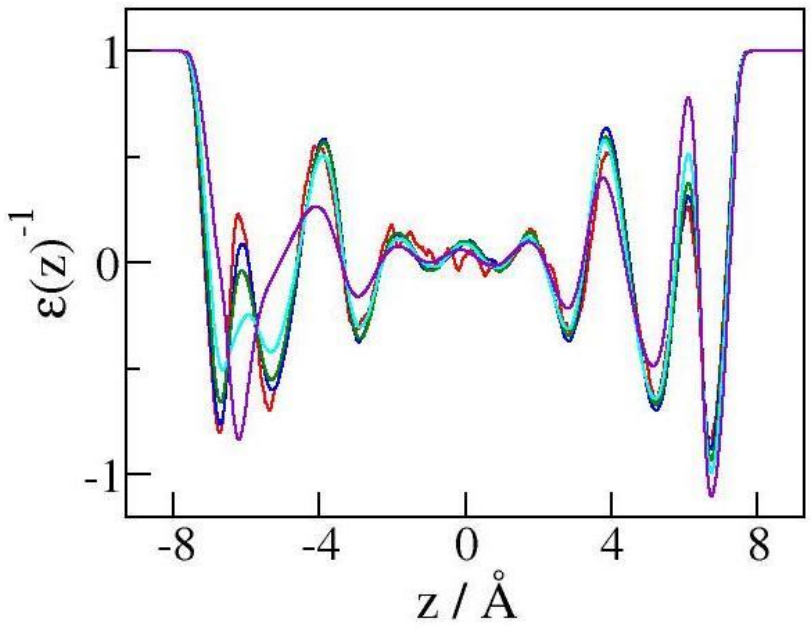

Fig. 5 The inverse of the normal component of dielectric constant $\bar{\varepsilon}(z)^{-1}$ across the nanopore at different voltages U (for color usage see Fig. 2).

width dependence of pore capacitance observed in ionic-liquid nanocapacitors[59, 60] should also apply to the aqueous ones. Fig. 5 presents the results for finite voltages considered in Figs. 2 and 3. Results for the remaining voltages are incorporated in Fig. S3 in the Supplementary Material.

In analogy with field-induced changes in layered charge density $\rho_q(z)$ and polarization change $\Delta m(z)$, (Figs. 3 and 4), the oscillations of $\frac{1}{\bar{\varepsilon}(z;U)}$ near the right wall (incoming field) visibly exceed those at the left side, suggesting enhanced regional overscreening and stronger overall dielectric response at the interface under incoming external field.

From a practical point of view, averages of $\frac{1}{\bar{\varepsilon}(z;U)}$ over distances above the lengthscales of molecular features are often of greater interest. In what follows, we turn attention to spatial averages $<\frac{1}{\bar{\varepsilon}(z;U)}>_l$ and $<\frac{1}{\varepsilon_d(z;U)}>_r$ taken over the left and right halves of the aqueous film. The film corresponds to the region of nonzero charge density (or number density of hydrogen atoms). Each half-space hence includes an entire hydration layer and one half of the bulklike aqueous interior while we exclude the inert layers with $\rho_q(z)$=0 and $\bar{\varepsilon}(z)$=1 on both sides of the film. Spatial averages (Fig. 6) are obtained by considering the total polarization M in the subvolume V_α corresponding to a region of the slab inside the simulation box of lateral dimensions L_x and L_y, bounded by planes at z_a and z_b

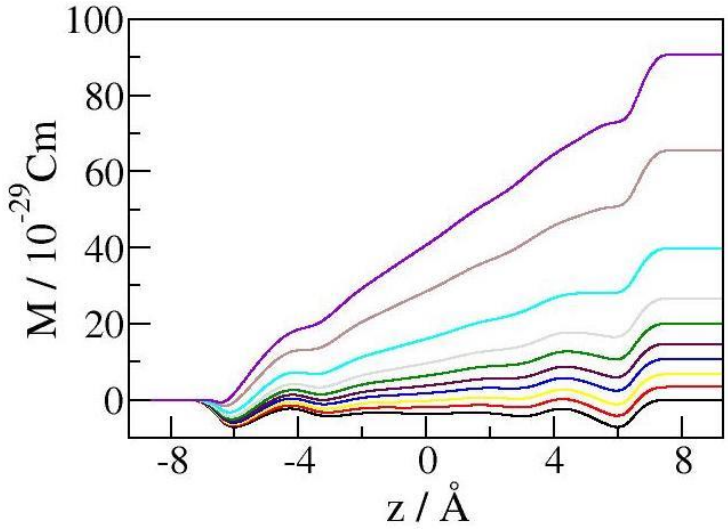

Fig. 6 Average dipole $M(z;U)$ associated with partial charges located in the simulation box at positions $z' \leq z$ for different voltages U across the pore. The colors corresponding to a set of values of U have the same meaning as in Fig. 4.

$$M_{ab} = L_x L_y \int_{z_a}^{z_b} m(z')dz' \,, \tag{7}$$

Fig. 6 shows the time-average of the dipole *M(z)* of the volume bounded by the left graphene sheet and a plane at a specified position z as a function of z for the set of voltages U considered in other figures. M_{ab} corresponding to the volume $V_{ab} = L_x L_y (z_b - z_a)$ for arbitrary choice z_a and z_b is equal to the increment of $M(z)$ (Fig. 6) between specified boundaries at z_a and z_b. The average inverse of the normal component of the dielectric difference constant in the region between z_a and z_b is

$$\frac{1}{\bar{\varepsilon}_{eff}} = < \frac{1}{\bar{\varepsilon}(z)} >_{ab} = 1 - \frac{<\Delta M_{ab}>}{V_{ab} E_o \varepsilon_o} \tag{8}$$

In the left half-space, z_a corresponds to the left boundary of the aqueous film and z_b to the box midplane (z_b=0); in calculation on the right, z_a=0 and z_b the r.h.s. boundary of the film.

The *inset* in Fig. 7 presents results for $\bar{\varepsilon}_{eff}(U)_l = < \frac{1}{\bar{\varepsilon}(U)} >_l^{-1}$ and $\bar{\varepsilon}_{eff}(U)_r = < \frac{1}{\bar{\varepsilon}(U)} >_r^{-1}$ in the two half-spaces as functions of the inter-plate voltage U. With the exception of very small voltages U corresponding to the linear response regime, the effective dielectric difference constant averaged over the right half-space (open green circles connected by dashed line) considerably exceeds its counterpart on the left side (open blue circles and blue dashed line). The difference initially increases with U, reaching its biggest value around $U \sim -0.6$ V and decreasing thereafter. This nonmonotonic behavior mirrors a similar trend of $\bar{\varepsilon}_{eff}(U)_r$, whose initial increase with U coincides with the field-induced reversal of the prevalent orientation of hydration molecules (the reversal only takes place under incoming field) [23]. The position of the maximum can be attributed to the balance between spontaneous angle bias of hydration molecules[23] and opposing alignment with the field at the right wall. If U is increased further, $\bar{\varepsilon}_{eff}(U)_r$ decreases following conventional dielectric saturation. No maximum of $\bar{\varepsilon}_{eff}(U)_l$ is observed at the left side where monotonic (bulklike) saturation behavior is observed over the entire voltage range. As hydration water molecules at the left wall favor dipole direction slightly away from the wall even without external field, saturation in the left compartment (in positive field E_o) is somewhat stronger than in bulk water.

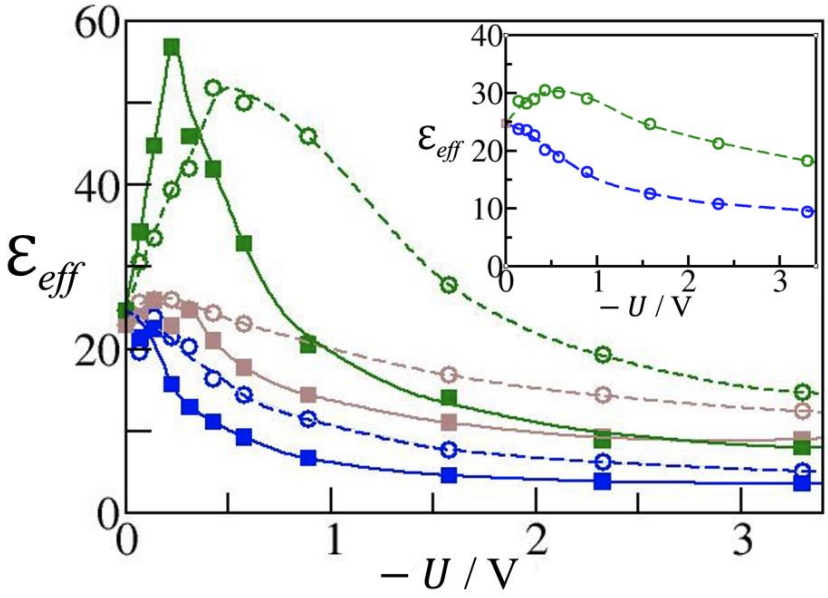

Fig. 7 The normal component of space-averaged dielectric difference constant ($\bar{\varepsilon}_{eff} = <\frac{1}{\bar{\varepsilon}(U)}>^{-1}$, open circles and dashed lines) and differential dielectric constants ($\varepsilon_{d,eff} = <\frac{1}{\varepsilon_d(U)}>^{-1}$, squares and solid lines) as functions of voltage U (the difference between electrostatic potentials on the opposing graphene sheets, $-U = \psi_{left} - \psi_{right}$). **Inset**: $\bar{\varepsilon}_{eff}$ averaged over the left (blue) and right (green) halves of the aqueous film. **Main plot**: averages over the entire width of the aqueous film (brown), the 1st hydration layer at the left wall where the field is pointing from the wall into the liquid (blue), and the 1st hydration layer at the right wall where the field is pointing from the liquid

The nonmonotonic variation of effective permittivity at modest field strengths followed by monotonic saturation at stronger fields bears resemblance with the change of the ion-free Stern layer permittivity extracted[61] from experiments[62] at a (negatively charged) silver electrode/NaF electrolyte surface. Because of its negative charge, the electrode resembles the right wall (green symbols in Fig. 7) of our model system. The experiment-based Stern layer dielectric constant follows the rescaled Kirkwood/Langevin saturation at strong fields while showing deviations at weaker ones[61]. Despite significant differences between the experimental and simulated system, both studies suggest a possible interplay between orienting wall/water bias and field-induced alignment as a possible source of deviation from conventional saturation in weak field. The deviation gradually disappears when the field becomes sufficiently strong to overwhelm the angle bias of interfacial molecules.

The left *vs.* right asymmetry is especially pronounced if we concentrate only on the first hydration layers next to graphene sheets. In the main graph in Fig. 7, we compare left and right averages, $\overline{\varepsilon}_{eff}^{h}(U)_l$ and $\overline{\varepsilon}_{eff}^{h}(U)_r$ over the width of the first hydration layer on each wall. The thickness of hydration layers is determined by the external boundaries of the aqueous film (~ 1.1 Å from either plate) and the positions of the first minimum of atomic density in the liquid, which are estimated at rounded values $z = \pm 4$ Å. Effective dielectric difference constants in both hydration layers, shown using the same colors and symbols as inside the inset of Fig. 6), feature qualitatively similar voltage dependences as the averages over entire half-spaces shown in the inset. Greater asymmetry between hydration layers confirms the difference between dielectric responses in two half-spaces is dominated by the contributions of the 1st hydration layers added to more equitable contributions from the interior of the slab. We also include effective dielectric difference constants of the entire aqueous film (brown circles and brown dashed curves in the main graph of Fig. 6). Combining the features of the left and right sides, the voltage dependence of the overall dielectric difference constant shows only mild maxima followed by expected saturation behavior.

We now turn attention to the comparison of *differential* dielectric constants for opposite hydration layers, $\varepsilon_d^h(U)_l$ and $\varepsilon_d^h(U)_r$. For this purpose, we seek averages of $\frac{1}{\varepsilon_d(z;U)}$ (Eq. 4) over the subvolumes V_α (α=*l* or *r* for the left or right hydration layer, respectively). Using the definitions of total polarization *M*, Eq 3, and regional polarizations M_{ab} , Eq. 7, the average of the inverse differential dielectric constant in the specified region between z_a and z_b with volume $V_{ab} = L_x L_y (z_b - z_a)$ is obtained from

$$\frac{1}{\varepsilon_{d,eff}} = < \frac{1}{\varepsilon_d(z)} >_{ab} = 1 - \frac{\beta}{V_{ab}\varepsilon_o} [\, <M_{ab}M> - <M_{ab}><M>] \qquad (9)$$

Applying Eq. 9 with the boundaries at z_a and z_b enveloping either of the hydration layers (see above) obtains effective differential dielectric constants $\varepsilon_{d,eff}^{h}(U)_l = < \frac{1}{\varepsilon_d(U)} >_l^{-1}$ and $\varepsilon_{d,eff}^{h}(U)_r = < \frac{1}{\varepsilon_d(U)} >_r^{-1}$ averaged over the left and right hydration layer. Simulation results for $\varepsilon_{d,eff}^{h}(U)_l$, $\varepsilon_{d,eff}^{h}(U)_r$, and those of the entire aqueous film, $\varepsilon_{d,eff}^{h}(U)$, are included in the main graph of Fig. 6 as solid squares and solid lines in blue, green, and brown color, respectively. These results reveal identical qualitative trends as the dielectric difference constant (open symbols and

dashed lines). Given the relation between $\bar{\varepsilon}$ and ε_d, Eq. 6, ε_d is expected to exceed $\bar{\varepsilon}$ when the latter quantity increases with the strength of applied field E_o (and voltage U), while $\bar{\varepsilon}$ should be bigger than ε_d in the dielectric saturation regime where $\bar{\varepsilon}$ decreases with U. These expectations agree with the voltage dependence of simulated dielectric constants shown in Fig. 7 and explain the shift of the maximum of ε_d (relative to the peak of $\bar{\varepsilon}$) to lower voltage U.

Despite quantitative differences, both ε_d and $\bar{\varepsilon}$ are strongly asymmetric and show bigger averaged values at the wall with the field pointing toward the solid. Asymmetric polarization inside a nanoscale capacitor will also modify the capacitor's performance under alternating (AC) voltage. Because of changing polarity, the time-averaged behaviors at the opposite interfaces will be symmetrized, however, we can expect a distorted local polarization response to a symmetrically oscillating applied voltage like *e.g.* the standard sinusoidal form. In view of the results shown in Fig.6, different polarization magnitudes are expected to take place in response to positive and negative signals irrespective of constant amplitude of the signal. Field polarity is also known to determine the dynamics of molecular reorientations at field-exposed interfaces[23, 51, 63]. Implications for dielectric responses to high frequency AC fields in nonlinear regime are being addressed in a parallel work to appear in a separate publication.

C. Inclusion of molecular polarizability

All results presented so far were obtained using the nonpolarizable SPC/E model for water. As estimated in previous studies with polarizable potentials of water, shielded external fields present in our systems do not themselves significantly polarize water molecules[64, 65], however, the molecules become polarized by much stronger, perpetually fluctuating *local* fields exerted by neighboring molecules. At surfaces, the latter effect is less prominent due to reduced water/water coordination[65-68]. To verify if molecular polarizability modifies the *polarity dependence* (relative to the wall) of dielectric response, we repeated the calculation of charge density (Fig. S5) and reciprocal dielectric constant profiles (Fig. S6), as well as effective dielectric difference constant averages for the two half-spaces, $\bar{\varepsilon}_{eff}(U)_l$ and $\bar{\varepsilon}_{eff}(U)_r$ and hydration layers using polarizable SWM4-NDP[37] model at one of the voltages from Table 1. $U \sim -0.225$ V (vacuum field E_o=0.08 VÅ^{-1}), was used as it showed the biggest polarity effect with the nonpolarizable force field. According to Figs. S5 and S6, simulated profiles of charge density $\rho_q(z)$ and $\frac{1}{\bar{\varepsilon}(z)}$ for the

polarizable and nonpolarizable model are qualitatively similar but show somewhat bigger oscillations of $\frac{1}{\bar{\varepsilon}(z)}$ with the polarizable model (Fig. S6). Both models reveal asymmetric responses to external field. In Table 2, we compare averages for the left and right half-spaces (robust with respect to dividing plane) and hydration layers (somewhat sensitive to plane positioning) from the

Table 2. Effective dielectric constants $\bar{\varepsilon}_{eff}(U)_l = <\frac{1}{\bar{\varepsilon}(U)}>_l^{-1}$ and $\bar{\varepsilon}_{eff}(U)_r = <\frac{1}{\bar{\varepsilon}(U)}>_r^{-1}$ averaged over left and right half-spaces of the aqueous film between graphene sheets at voltage $U \sim -0.23$ V for nonpolarizable (SPC/E) and polarizable (SWM4-NDP) models of water. Estimated uncertainties of $\bar{\varepsilon}_{eff}$ are up to ± 0.5.

model	left half	left hydration layer	entire film	right half	right hydration layer
SPC/E	24.4	22	26.2	28.3	39
SWM4-NDP	20	14	23	26	19

two models. While bulk SWM4-NDP water[37] has higher dielectric constant than SPC/E[36] (79 ± 3 *vs.* 68 ± 2), the opposite holds true in the confinement (average $\bar{\varepsilon}_{eff}$ in water film 23 ± 1 *vs.* 26.2 ± 1) and the reduction is most visible in the hydration layers. The difference is explained in terms of lower mean dipoles of polarizable molecules with incomplete coordination (~1.85 D for isolated SWM4-NDP molecule vs. ~2.46 D in the bulk phase). *Ab initio*[67, 68] and

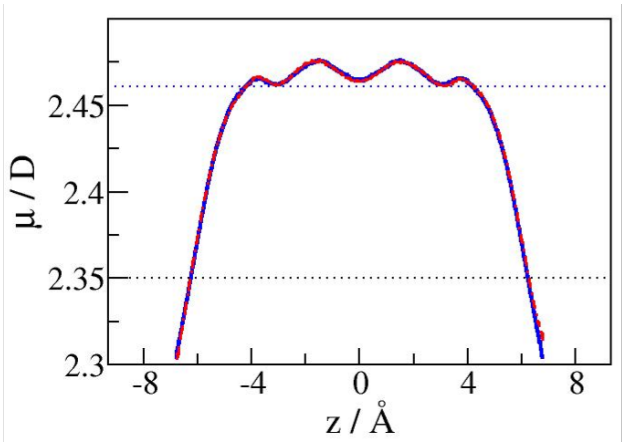

Fig. 8 Average dipole of confined SWM4-NDP molecules as a function of position z at zero voltage (solid blue line) or at U=-0.225 V (dashed red line). Confining walls are at z=±9.31 Å. Horizontal dotted lines at 2.35 D and 2.461 D correspond to bulk dipoles of SPC/E and SWM4-NDP models, respectively.

classical polarizable models of interfacial water[65, 66, 68] typically show about 10% smaller dipole moments than inside the bulk phase. In Fig. 8, we show the position (z) dependence of the average dipole in confined SWM4-NDP water at zero voltage and at U=-0.225 V. Here, external field has almost no effect, however, a dipole reduction of up to 8% is observed at the film surfaces. While we defer a detailed analysis of molecular polarizability to future work, we note that essentially the same polarity dependence is observed in both the nonpolarizable and polarizable representations, with effective interfacial permittivities under incoming field consistently exceeding the permittivities at the opposite wall under outgoing direction of the field.

IV. Concluding remarks

Structure of interfacial water under electric perturbation has been known to depend on the direction of electric field relative to the confinement walls. In a planar confinement subject to perpendicular field this leads to different properties of hydration water at opposing surfaces. Our Molecular Dynamics study manifests the emergence of distinct dielectric responses at interfaces under incoming and outgoing fields in the nonlinear response regime. The asymmetry between effective dielectric constants at opposite walls is mostly due to a nonmonotonic field dependence of water permittivity within the hydration layer under incoming (pointing from liquid to wall) electric field. Contrary to the conventional saturation behavior, here the differential dielectric constant initially *increases* with the field, passing through a maximum at field strength sufficient to approximately balance the orientational bias of interfacial water molecules due to hydrogen bonding. Further increase in field strength results in gradual dielectric saturation and diminishing dielectric contrast between the two walls. The voltage dependence of the dielectric difference constant resembles that of the differential dielectric constant with the maximum shifted to about twice stronger voltage. The interior of the confined aqueous film, as well as the hydration water at the opposite wall (under outgoing field), shows monotonic saturation similar to the bulk aqueous phase. The dependence of dielectric difference constant on field polarity (relative to adjacent confinement wall) remains similar after inclusion of molecular polarizability of water. By offsetting the angle bias of surface water molecules, the field maximizing the average permittivity next to the wall under incoming field has also been shown[23] to smooth the reorientational landscape

and accelerate rotation dynamics of interfacial molecules. Implications for capacitor performance under high frequency AC fields (0.1-10 THz) will be reported in a parallel study.

Supplementary material

Supplementary material presents structural and polarization profiles at additional voltages and compares total polarization to pure dipolar contribution in SPC/E water. It also includes a comparison of charge density and inverse dielectric constant profiles based on nonpolarizable (SPC/E) and polarizable (SWM4-NDP) models of water in a nanoconfinement.

Acknowledgment

We acknowledge National Science Foundation for support (award CHE-1800120), and National Energy Research Scientific Computing Center (NERSC), funded by the Office of Science of the U.S. Department of Energy (No. DEAC02-05CH11231) and Extreme Science and Engineering Discovery Environment (XSEDE), funded by NSF Grant No. OCI-1053575 for supercomputing time allocations.

Conflicts of interest

The authors have no conflicts to disclose.

References:

(1) K. Morikawa, Y. Kazoe, K. Mawatari, T. Tsukahara, and T. Kitamori, *Anal. Chem.* **87**, 1475 (2015).
(2) B. Natarajan, C. Emiroglu, J. Obrzut, D. M. Fox, B. Pazmino, J. F. Douglas, and J. W. Gilman, *ACS Appl. Mat. Interfaces* **9**, 14222 (2017).
(3) L. Fumagalli, A. Esfandiar, R. Fabregas, S. Hu, P. Ares, A. Janardanan, Q. Yang, B. Radha, T. Taniguchi, K. Watanabe, G. Gomila, K. S. Novoselov, and A. K. Geim, *Science* **360**, 1339 (2018).
(4) A. Montenegro, C. Dutta, M. Mammetkuliev, H. T. Shi, B. Y. Hou, D. Bhattacharyya, B. F. Zhao, S. B. Cronin, and A. V. Benderskii, *Nature* **594**, 62 (2021).
(5) D. J. Bonthuis, S. Gekle, and R. R. Netz, *Phys. Rev. Lett.* **107**, 166102 (2011).
(6) S. Gekle, and R. R. Netz, *J. Chem. Phys.* **137**, 104704 (2012).
(7) S. Varghese, S. K. Kannam, J. S. Hansen, and S. P. Sathian, *Langmuir* **35**, 8159 (2019).
(8) M. H. Motevaselian, and N. R. Aluru, *ACS Nano* **14**, 12761 (2020).
(9) M. Rezaei, B. G. Mitterwallner, P. Loche, Y. Uematsu, R. R. Netz, and D. J. Bonthuis, *J. Phys. Chem. B* **125**, 4767 (2021).
(10) D. V. Matyushov, *J. Phys. Chem. B* **125**, 8282 (2021).
(11) S. J. Cox, and P. L. Geissler, *Chem. Sci.* **13**, 9102 (2022).
(12) G. Gonella, E. H. G. Backus, Y. Nagata, D. J. Bonthuis, P. Loche, A. Schlaich, R. R. Netz, A. Kuhnle, I. T. McCrum, M. T. M. Koper, M. Wolf, B. Winter, G. Meijer, R. K. Campen, and M. Bonn, *Nature Rev. Chem.* **5**, 466 (2021).
(13) J. F. Olivieri, J. T. Hynes, and D. Laage, *J. Phys. Chem. Lett.* **12**, 4319 (2021).
(14) S. Senapati, and A. Chandra, *J. Phys. Chem. B* **105**, 5106 (2001).

(15) D. J. Bonthuis, S. Gekle, and R. R. Netz, *Langmuir* **28**, 7679 (2012).
(16) E. Papadopoulou, J. Zavadlav, R. Podgornik, M. Praprotnik, and P. Koumoutsakos, *ACS Nano* **15**, 20311 (2021).
(17) S. Mondal, and B. Bagchi, *J. Phys. Chem. Lett.* **10**, 6287 (2019).
(18) S. Mondal, and B. Bagchi, *J. Chem. Phys.* **154**, 044501 (2021).
(19) S. De Luca, S. K. Kannam, B. D. Todd, F. Frascoli, J. S. Hansen, and P. J. Daivis, *Langmuir* **32**, 4765 (2016).
(20) S. Ruiz-Barragan, D. Munoz-Santiburcio, S. Korning, and D. Marx, *Phys. Chem. Chem. Phys.* **22**, 10833 (2020).
(21) M. Neumann, *J. Chem. Phys.* **85**, 1567 (1986).
(22) I. C. Yeh, and M. L. Berkowitz, *J. Chem. Phys.* **110**, 7935 (1999).
(23) M. von Domaros, D. Bratko, B. Kirchner, and A. Luzar, *J. Phys. Chem. C* **117**, 4561 (2013).
(24) C. Y. Lee, J. A. McCammon, and P. J. Rossky, *J. Chem. Phys.* **80**, 4448 (1984).
(25) A. Luzar, S. Svetina, and B. Zeks, *J. Chem. Phys.* **82**, 5146 (1985).
(26) J. C. Shelley, and G. N. Patey, *Mol. Phys.* **88**, 385 (1996).
(27) D. Bratko, C. D. Daub, K. Leung, and A. Luzar, *J. Am. Chem. Soc.* **129**, 2504 (2007).
(28) D. Bratko, C. D. Daub, and A. Luzar, *Faraday Discuss.* **141**, 55 (2009).
(29) C. D. Daub, D. Bratko, and A. Luzar, *Top. Curr. Chem.* **307**, 155 (2012).
(30) N. Ojaghlou, D. Bratko, M. Salanne, M. Shafiei, and A. Luzar, *ACS Nano* **14**, 7987 (2020).
(31) W. Humphrey, A. Dalke, and K. Schulten, *J. Mol. Graph.* **14**, 33 (1996).
(32) F. Moucka, D. Bratko, and A. Luzar, *J. Phys. Chem. C* **119**, 20416 (2015).
(33) J. R. Choudhuri, D. Vanzo, P. A. Madden, M. Salanne, D. Bratko, and A. Luzar, *ACS Nano* **10**, 8536 (2016).
(34) D. Vanzo, D. Bratko, and A. Luzar, *J. Phys. Chem. B* **119**, 8890 (2015).
(35) H. J. C. Berendsen, J. R. Grigera, and T. P. Straatsma, *J. Phys. Chem.* **91**, 6269 (1987).
(36) C. Vega, and J. L. F. Abascal, *Phys. Chem. Chem. Phys.* **13**, 19663 (2011).
(37) G. Lamoureux, E. Harder, I. V. Vorobyov, B. Roux, and A. D. MacKerell, *Chem. Phys. Lett.* **418**, 245 (2006).
(38) D. Vanzo, D. Bratko, and A. Luzar, *J. Chem. Phys.* **137**, 034707 (2012).
(39) J. Driskill, D. Vanzo, D. Bratko, and A. Luzar, *J. Chem. Phys.* **141**, 18C517 (2014).
(40) D. Bratko, R. A. Curtis, H. W. Blanch, and J. M. Prausnitz, *J. Chem. Phys.* **115**, 3873 (2001).
(41) F. Moucka, D. Bratko, and A. Luzar, *J. Chem. Phys.* **142**, 124705 (2015).
(42) D. Van der Spoel, E. Lindahl, B. Hess, G. Groenhof, A. E. Mark, and H. J. C. Berendsen, *J. of Comput. Chem.* **26**, 1701 (2005).
(43) T. Darden, D. York, and L. Pedersen, *J. Chem. Phys.* **98**, 10089 (1993).
(44) G. Bussi, D. Donadio, and M. Parrinello, *J. Chem. Phys.* **126**, 014101 (2007).
(45) I. C. Yeh, and M. L. Berkowitz, *J. Chem. Phys.* **111**, 3155 (1999).
(46) V. Ballenegger, A. Arnold, and J. J. Cerda, *J. Chem. Phys.* **131**, 094107 (2009).
(47) B. Hess, H. Bekker, H. J. C. Berendsen, and J. Fraaije, *J. Comput. Chem.* **18**, 1463 (1997).
(48) B. Hess, *J. Chem. Theory Comput.* **4**, 116 (2008).
(49) M. A. Saitta, F. Saija, and P. Giaquinta, *Phys. Rev. Lett.* **108**, 207801 (2012).
(50) E. M. Stuve, *Chem. Phys. Lett.* **519-20**, 1 (2012).

(51) Y. W. Zhang, H. B. de Aguiar, J. T. Hynes, and D. Laage, *J. Phys. Chem. Lett.* **11**, 624 (2020).
(52) J. I. Siepmann, and M. Sprik, *J. Chem. Phys.* **102**, 511 (1995).
(53) S. K. Reed, O. J. Lanning, and P. A. Madden, *J. Chem. Phys.* **126** (2007).
(54) V. Ballenegger, and J. P. Hansen, *J. Chem. Phys.* **122**, 114711 (2005).
(55) H. Itoh, and H. Sakuma, *J. Chem. Phys.* **142**, 184703 (2015).
(56) D. J. Bonthuis, and R. R. Netz, *J.Phys. Chem. B* **117**, 11397 (2013).
(57) A. Schlaich, E. W. Knapp, and R. R. Netz, *Phys. Rev. Lett.* **117**, 048001 (2016).
(58) Y. C. Gan, and W. Q. Cao, *Ferroel. Lett. Sect.* **47**, 96 (2020).
(59) G. Feng, and P. T. Cummings, *J. Phys. Chem. Lett.* **2**, 2859 (2011).
(60) D. E. Jiang, Z. H. Jin, and J. Z. Wu, *Nano Lett.* **11**, 5373 (2011).
(61) X. P. Wang, K. Liu, and J. Z. Wu, *J. Chem. Phys.* **154**, 124701 (2021).
(62) G. Valette, *J. Electroanal. Chem.* **122**, 285 (1981).
(63) G. Stirnemann, P. J. Rossky, J. T. Hynes, and D. Laage, *Faraday Discuss.* **146**, 263 (2010).
(64) M. Shafiei, M. von Domaros, D. Bratko, and A. Luzar, *J. Chem. Phys.* **150**, 074505 (2019).
(65) F. Moucka, S. Zamfir, D. Bratko, and A. Luzar, *J. Chem. Phys.* **150**, 164702 (2019).
(66) L. X. Dang, and T. M. Chang, *J. Chem. Phys.* **106**, 8149 (1997).
(67) I. F. W. Kuo, and C. J. Mundy, *Science* **303**, 658 (2004).
(68) C. J. Mundy, and I. F. W. Kuo, *Chem. Rev.* **106**, 1282 (2006).